RSC Advances

ROYAL SOCIETY OF CHEMISTRY

PAPER

View Article Online
View Journal | View Issue

Cite this: *RSC Adv.*, 2026, **16**, 23651

Synthesis, characterization, and catalytic performance in 1-butene cracking of ZSM-5 zeolites prepared with different cross-linked silicon species

Zhen Chen, *[a] Jingfei Geng,[a] Xiaofang Chen,[b] Na Li,[a] Richuan Rao,[a] Xiongzi Dong,[a] Haiping Zou[cd] and Weihang Ou[a]

Received 24th October 2025
Accepted 28th April 2026

DOI: 10.1039/d5ra08160b

rsc.li/rsc-advances

ZSM-5 zeolites were prepared *via* a hydrothermal synthesis approach, wherein the alkalinity of the synthesis system was precisely regulated to achieve directional control over the cross-linked configuration of silicon species. XRD, XPS, and ^{27}Al MAS NMR techniques were employed to conduct comprehensive characterization of the synthesized ZSM-5 zeolite, followed by a systematic evaluation of its catalytic performance in the conversion of 1-butene to propylene *via* catalytic cracking. The results demonstrated that low alkalinity conditions favored the formation of silicon species with low cross-linking, whereas high alkalinity conditions facilitated the generation of highly cross-linked silicon species. Leveraging this insight, C-series and T-series ZSM-5 zeolites were successfully synthesized using highly cross-linked and low cross-linked silicon species as silicon sources, respectively. Compared to T-series ZSM-5 zeolites, C-series zeolites exhibited lower acid strength, reduced Brønsted acid site density, fewer structural defects, and a more uniform distribution of framework aluminum. These inherent properties conferred superior catalytic selectivity. Notably, when employed in the catalytic cracking of 1-butene to propylene, C-series zeolites achieved an impressive 55% propylene selectivity, demonstrating significant potential for industrial applications.

1. Introduction

Propylene and its downstream derivatives exhibit considerable industrial application value, with the development of high-selectivity propylene production technologies representing a current frontier focus in international research.[1,2] Currently, the principal industrial processes for propylene production encompass steam cracking, methanol-to-olefins (MTO) and fluid catalytic cracking (FCC).[3,4] Nevertheless, these conventional production methods are commonly constrained by technical limitations, including the substantial co-production of C_4 olefins and relatively low propylene yields.[5,6] As an advanced integration of steam cracking and catalytic cracking technologies, catalytic cracking offers distinct advantages, including broad feedstock flexibility, superior product selectivity, streamlined process configuration, reduced reaction temperature requirements, and enhanced olefin production efficiency.[7–10] This technology has been widely adopted in large-scale low-carbon olefin cracking for propylene production, including processes such as KBR's Superflex,[11] UOP's Olefin Cracking Process (OCP),[12] Asahi Kasei's Omega process,[13] and Sinopec's OCC process.[14,15] The primary challenge currently confronting low-carbon olefin catalytic cracking technology lies in minimizing non-olefin by-products while simultaneously enhancing olefin yield—particularly the target product propylene—without compromising high raw material conversion rates. The development of highly efficient catalysts constitutes a pivotal factor in solid acid catalytic reactions.

Owing to its distinctive three-dimensional pore architecture and outstanding thermal and hydrothermal stability, ZSM-5 zeolite has emerged as a benchmark catalytic material for the cracking of 1-butene to yield low-carbon olefins.[16,17] During the catalytic reaction, its performance is primarily governed by key parameters including the acid strength, acid density, and spatial distribution of acid sites on the zeolite.[16,18,19] Lin *et al.*[18] synthesized a series of ZSM-5 zeolites (Z-1 to Z-5) featuring comparable acid densities but systematically varied acid strength gradients, and conducted a comprehensive investigation into the effects of acid strength on the catalytic cracking of 1-butene. The findings revealed that an increase in acid strength led to a significant reduction in propylene selectivity, accompanied by a notable enhancement in the yields of both alkanes and aromatic hydrocarbons. Zhu *et al.*[16] investigated the influence of acid site density in ZSM-5 zeolites with varying Si/Al ratios on the product

---

[a] *Pollution Control Research Institute of Pharmaceutical Wastewater, Hefei Normal University, Hefei, Anhui, 230601, China. E-mail: 2992206151@qq.com*
[b] *Ganzhou Vocational and Technical College, Ganzhou, 341003, China*
[c] *Jiangxi Qianyue New Materials Co., Ltd, Ganzhou, 341003, China*
[d] *School of Rare Metal Industries, Hejun College, Ganzhou 342600, China*

selectivity of butene cracking. Their findings revealed that while increasing the Si/Al ratio (corresponding to a decrease in acid site density) led to a slight reduction in butene conversion, it simultaneously resulted in a significant enhancement in the combined selectivity of ethylene and propylene. Zhang *et al.*[19] synthesized a series of ZSM-5 zeolites with varied acid distribution properties through calcium nitrate modification, demonstrating that preserving the acid sites on the external zeolite surface significantly enhanced the reaction selectivity for propylene production during 1-butene cracking. Current research primarily employs post-treatment methods—such as phosphorus (P) modification,[20,21] alkali metal modification,[22,23] alkaline earth metal modification,[24] and rare earth element modification[25,26]—to regulate the acidity of zeolites for the development of 1-butene cracking catalysts with enhanced olefin selectivity. However, these modification strategies remain largely empirical, lacking a systematic framework and relying predominantly on trial-and-error optimization.

Currently, the synthesis of ZSM-5 zeolite predominantly employs the hydrothermal synthesis method. During this process, silicon species form the primary framework of the zeolite, the polymerization state of silicate anions and their structural evolution persist throughout the entire gelation and crystallization stages of ZSM-5 zeolite formation. The structural characteristics inherently influence the incorporation behaviour of Al atoms into the framework. Burkett[27] systematically classified the diverse silicate species potentially present in the precursor suspensions of high-silica zeolites. It is widely acknowledged that the polymerization and depolymerization of silicon species exist in a dynamic equilibrium, with the specific molecular configurations of silicon species in solution being governed by key parameters including pH value, reaction temperature, template agent selection, and their respective concentrations.[28–31] From the perspective of regulating silicon species structure, our research team[32,33] proposed an efficient synthesis strategy for heteroatomic zeolites, developing two distinct synthetic approaches: a "top-down" and a "bottom-up" route. The synthesized TS-1 zeolite was applied to investigate the molecular traffic control (MTC) effect in shape-selective catalysis,[34] while the ZSM-5 zeolite was employed to study the methanol-to-olefins (MTO) reaction.[35] In this study, silicon species with varying degrees of cross-linking were synthesized as silicon precursors *via* a "top-down" approach, and subsequently utilized in conjunction with $NaAlO_2$ as the aluminium source to prepare a series of ZSM-5 zeolites. The influence of the cross-linking state of silicon species on the acidic properties and pore architecture of ZSM-5 zeolites was comprehensively examined employing a range of characterization techniques, followed by an in-depth investigation into their catalytic behaviour in the butene-to-propylene cracking reaction.

2. Experimental

2.1. Preparation of silicon species precursor

Firstly, the mixed sol was prepared with a molar ratio of $1.0SiO_2 : 0.2TPAOH : 34H_2O$. The detailed synthesis procedure was conducted as follows: a precisely measured 1.0 g sample of S-1 zeolite (preparation methodology detailed in the SI) was thoroughly homogenized with 2.715 g of a 25 wt% tetrapropyl ammonium hydroxide (TPAOH) aqueous solution and 8.220 g of deionized water. The resulting homogeneous mixture was subsequently transferred to a stainless-steel sealed crystallization autoclave, which was then placed in a thermostatically controlled stirred autoclave reactor system. The process was performed under dynamic heating conditions at 443 K (170 °C) for a standardized duration of 3 hours. Upon reaching the predetermined time, the crystallization kettle was carefully removed and allowed to cool naturally to ambient temperature, yielding silicon species A. Meanwhile, another mixed sol with a molar ratio of $1.0SiO_2 : 1.0TPAOH : 34H_2O$ was prepared. The specific experimental procedure was as follows: A quantity of 1.00 g of S-1 zeolite was accurately weighed and subsequently combined with 13.557 g of a 25 wt% aqueous TPAOH solution at ambient temperature, followed by thorough mechanical stirring to ensure homogeneous mixing. The subsequent operational procedures—including the transfer to the crystallization kettle, heating parameters, and cooling methodology—were strictly identical to those employed in the preparation of silicon species A. This process ultimately yielded silicon species B. The synthesized silicon species A and B were then collected for comprehensive characterization.

2.2. Synthesis of ZSM-5 zeolites

The ZSM-5 zeolite was synthesized using the aforementioned silicon sources (species A and B) with $NaAlO_2$ serving as the aluminium source. The Si/Al molar ratios of the reaction feed were controlled at 50 and 100, respectively. After thoroughly mixing the silicon source and aluminium source, the resulting homogeneous sol was transferred into a stainless steel crystallization autoclave, where it underwent dynamic crystallization at 443 K for 48 hours. After the crystallization process was completed, the crystallization kettle was removed and rapidly cooled to room temperature using an ice-water bath. Subsequently, suction filtration was performed, followed by washing with deionized water. The resulting filter cake was dried overnight in a thermostatically controlled oven at 333 K to yield the Na-ZSM-5 zeolite. Subsequently, the Na-ZSM-5 zeolite underwent an ion exchange process *via* the ammonium exchange method (with a mass ratio of zeolite : $NH_4Cl : H_2O = 1 : 1 : 15$), yielding hydrogen-form ZSM-5 zeolite. Product naming based on silicon source type and feeding ratio: samples prepared with silicon species A as the silicon source were labeled as T-50 (the starting materials molar ratio of Si/Al is 50, actual Si/Al = 50 as determined by ICP) and T-94 (the starting materials molar ratio of Si/Al is 100, actual Si/Al = 94 as determined by ICP); the samples prepared using silicon species B as the silicon source were labeled as C-47 (the starting materials molar ratio of Si/Al is 50, actual Si/Al = 47 as determined by ICP) and C-101 (the starting materials molar ratio of Si/Al is 100, actual Si/Al = 101 as determined by ICP).

2.3. Characterizations of ZSM-5 zeolites

A comprehensive suite of advanced characterization techniques—including X-ray diffraction (XRD), inductively coupled plasma atomic emission spectroscopy (ICP), scanning electron microscopy (SEM), X-ray photoelectron spectroscopy (XPS), solid-state ^{29}Si magic-angle spinning nuclear magnetic resonance (^{29}Si MAS NMR), solution-state ^{29}Si NMR, ammonia temperature-programmed desorption (NH_3-TPD), solid-state ^{27}Al MAS NMR, pyridine adsorption coupled with IR spectroscopy (Py-IR), Fourier transform infrared spectroscopy (FT-IR) and nitrogen adsorption–desorption analysis (BET)—was employed to systematically investigate the cross-linking states of silicon species and the physicochemical properties of the synthesized ZSM-5 zeolite. Detailed information on the instrumentation used, including instrument types, specifications, and testing parameters, is provided in the SI.

2.4. 1-Butene catalytic cracking reaction

The 1-butene catalytic cracking reaction was experimentally investigated using the HPMR-1542 high-pressure microreactor chromatography system (Beijing Weikendu Technology Co., Ltd). The reaction tube consisted of a copper-plated iron core housed within a stainless steel outer tube with an inner diameter of 10 mm. A thermocouple was inserted into the catalyst bed through a protective thin-walled tube. The catalyst (1.0 g) was loaded into the stainless steel reaction tube after being mechanically treated (compressed, crushed, and sieved) to a particle size range of 0.250–0.425 mm. Prior to the reaction, the catalyst was pretreated under a nitrogen atmosphere by heating at 823 K for 4 h, followed by nitrogen flow activation (180 mL min^{-1}) at 823 K for 3 h. The reaction feedstock consisted of 1-butene with a purity of 99.9%. During the reaction, 1-butene was diluted with nitrogen at an N_2/C_4H_8 molar ratio of 7.82. Product identification and quantification were performed using an Agilent GC7890A gas chromatograph equipped with multiple columns: an Agilent 19095P-M25 (50 m × 530 μm × 15 μm) column, Dikma 2 m × 1/85 A column, Dikma 2 m × 1/8 Porapak Q column, as well as two Dikma 1 m × 1/8 Porapak Q columns and FID detectors for detecting the content and type of hydrocarbon components, and two TCD detectors for detecting the content of hydrogen and nitrogen. Although the feedstock consisted of pure 1-butene, the butene conversion was calculated based on the total butene isomers (1-, 2-, *cis*-2-, and *trans*-2-butene) presented in the system to ensure an accurate representation of the cracking mechanism. The relevant calculation formulas are presented in the SI.

3. Results and discussion

3.1. Characterization of cross-linking state of silicon species

Fig. 1 presents the FT-IR infrared spectra of TPAOH aqueous solution, as well as silicon species A and B. The peaks observed at 1650 cm^{-1}, 1460–1490 cm^{-1}, and 970 cm^{-1} correspond to the vibrational modes associated with chemical bonds in the TPAOH aqueous solution. The FT-IR spectra of silicon species A and B exhibit dominant absorption peaks at approximately 1100 cm^{-1} and 1000 cm^{-1}, respectively, which are attributed to the stretching vibrations of the Si–O–Si species.[29,30] In conjunction with the relevant literature,[35] it can be further elucidated that silicon species A, obtained by dissolving S-1 zeolite under low alkalinity conditions ($TPAOH/SiO_2 = 0.2$), predominantly exists in a low-crosslinked silicon form, whereas silicon species B, derived from S-1 zeolite dissolution under high alkalinity conditions ($TPAOH/SiO_2 = 1.0$), primarily adopts a highly cross-linked structural state.

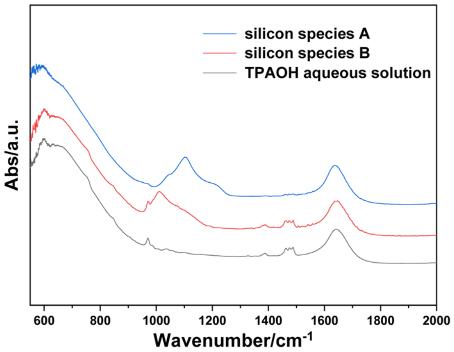

Fig. 1 FT-IR spectra of silicon species A, silicon species B and TPAOH aqueous solution.

The literature[27,32] demonstrates that in the ^{29}Si NMR spectrum, the resonance peak with a chemical shift ranging from −68 to −76 ppm corresponds to a monomeric silicon species [designated as Q^0]. The peak observed at −80 to −81.3 ppm is attributed to a dimeric silicon species [labeled $Q^{1\text{-d}}$]. The signal at −80.8 to −82.7 ppm is assigned to the terminal silicon species within a chain-like silicate framework [denoted as $Q^{1\text{-c}}$]. The Q^2 species, characterized by chemical shifts between −82 and −92 ppm, represents silicon atoms bridged to two additional silicon centers *via* Si–O–Si linkages. The Q^3 species, with resonances in the range of −92 to −100 ppm, corresponds to silicon atoms linked to three neighboring silicon atoms through oxygen bridges. Finally, the Q^4 species, exhibiting signals at −100 to −115 ppm, constitutes the fully condensed, three-dimensionally cross-linked silicate framework. The peaks in the ^{29}Si NMR spectra of silicon species A and B are labeled in Fig. 2, meanwhile Table S1 summarizes the ratio of peak areas for Q^1–Q^3 species relative to the Q^0 species in their respective ^{29}Si NMR spectra. Collectively, the data presented in Fig. 2 and Table S1 reveal that silicon species B—obtained by dissolving S-1 zeolite under high alkalinity conditions ($TPAOH/SiO_2 = 1.0$)—exists in a diverse array of chemical environments, dominated by Q^0, Q^1, Q^2, and Q^3 structural units. In contrast, silicon species A, obtained under milder alkaline conditions ($TPAOH/SiO_2 = 0.2$), exhibits fewer NMR signals with lower intensities. This spectral behaviour indicates a simpler structural architecture and a more constrained range of silicon chemical environments, which is primarily composed of monomeric Q^0 species and $Q^{1\text{-d}}$ species.

3.2. Characterization of ZSM-5 zeolites

XRD analysis is employed to investigate the phase composition of ZSM-5 zeolite synthesized with varying cross-linked silicon species. The resulting XRD patterns (Fig. 3) reveal that all four samples exhibit characteristic diffraction peaks at $2\theta = 7.96°$,

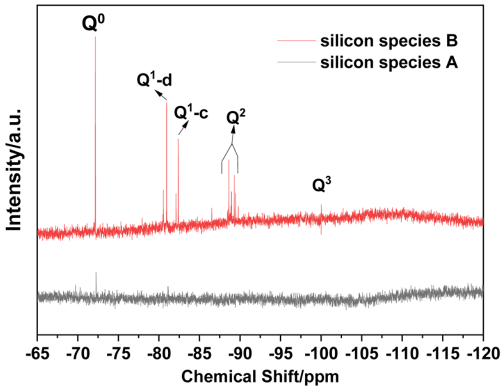

Fig. 2 ^{29}Si NMR spectra of silicon species A and B.

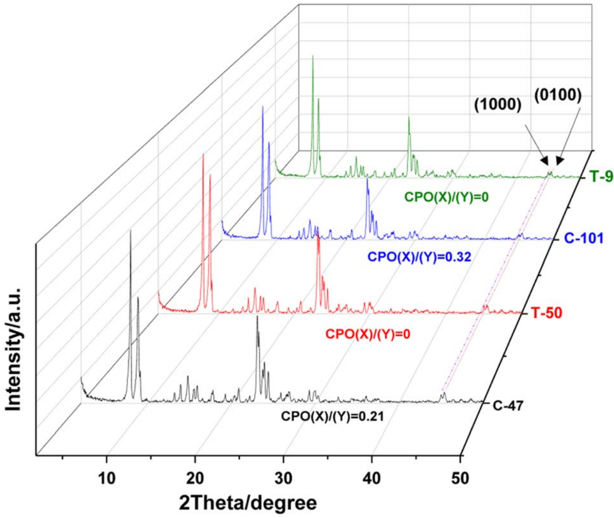

Fig. 3 XRD patterns of C-series and T-series ZSM-5 zeolites.

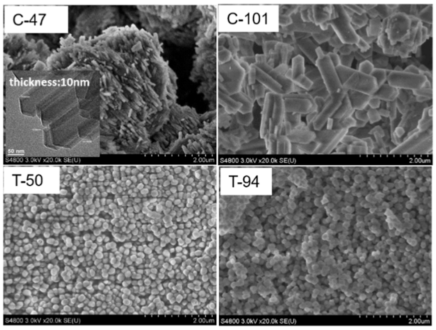

Fig. 4 SEM images of C-series and T-series ZSM-5 zeolites.

8.83°, 23.18°, 23.99°, and 24.45°, which are indicative of the ZSM-5 zeolite phase.[36] These results confirm the successful synthesis of ZSM-5 zeolites with well-defined MFI topology and high crystallinity using both highly cross-linked and lowly cross-linked silicon species as precursors. Fig. 3 also shows that the relative intensities of the diffraction peaks at angles of 45.09° and 45.64° are different for C series and T series ZSM-5 zeolites. As reported in the literature,[37] the Crystallographic Preferred Orientation (CPO) index—a parameter for characterizing and quantitatively comparing anisotropic growth along distinct crystallographic axes of MFI-type crystals—is defined as $I_S^{(X)}/I_S^{(Y)}$ minus $I_P^{(X)}/I_P^{(Y)}$, and then divided by $I_S^{(X)}/I_S^{(Y)}$. Here, P denotes the reference sample, consisting of finely powdered zeolite with random crystal orientation, while S represents the as-synthesized zeolite crystals under investigation, which exhibit a regular prismatic morphology. The ratio of the intensity for (1000) diffraction peak at ($I(X)$) 45.64°/2θ to the intensity of (0100) diffraction peak ($I(Y)$) at 45.09°/2θ[36] in the XRD pattern of the reference sample and the investigated sample is used to calculate the index of CPO(X)/(Y), respectively. The CPO(X)/(Y) index quantifies the relative growth extent of zeolite crystals along the *a*-axis *versus* the *b*-axis. A negative CPO(X)/(Y) value indicates that the MFI-type zeolite crystals exhibit a preferential orientation along the *a*-axis. Conversely, a positive CPO(X)/(Y) value corresponds to a coffin-shaped morphology, where the crystals are thicker along the *a*-direction and thinner along the *b*-direction, with the (0100) crystal face being significantly larger than the (1000) face. Sample T-94 or sample T-50, the MFI zeolite crystallites without preferred orientation is used as the reference. As shown in Fig. 3, the CPO(X)/(Y) values of zeolites C-47 and C-101 are 0.21 and 0.32, respectively. These results suggest that, in contrast to the T-series zeolites, the C-series zeolites display a preferential orientation along the *b*-axis.

As illustrated in Fig. 4, ZSM-5 zeolites synthesized with high and low cross-linking silicon species demonstrate distinctly different morphological characteristics. Specifically, the T-94 and T-50 zeolites prepared from low-crosslinked silicon species exhibit a small blueberry-like morphology. In contrast, the C-101 and C-47 zeolites derived from highly cross-linked silicon species display a *b*-axis oriented flat plate structure. Notably, the C-101 zeolite demonstrates a relatively larger crystal size.

Literature research indicates that BET analysis reveals that the sample exhibits type IV adsorption–desorption isotherms and type H3 hysteresis loops, signifying the presence of interparticle mesoporous structures formed *via* nanoparticle aggregation.[38] As illustrated in Fig. 5, N_2 adsorption–desorption isotherms of T-94 and T-50 zeolites display characteristic type IV behaviour, accompanied by type H3 hysteresis loops in the relative pressure range (P/P^0) of 0.8–0.9, thereby confirming their pronounced mesoporous structural features. This pore architecture substantially enhances nitrogen adsorption capacity through the capillary condensation mechanism, aligning with their high external specific surface area ($S_{\text{exter.}} = 68.7–83.1\ \text{m}^2\ \text{g}^{-1}$) and total pore volume ($V_{\text{total}} = 0.48–0.52\ \text{cm}^3\ \text{g}^{-1}$) (detailed in SI, Table S2). In contrast, the BET curve of the C-series zeolites (C-101, C-47) exhibits a type I pattern, indicative of a micropore-dominated pore structure. As shown in Fig. S1 and Table S2, the surface area, external specific surface area, total pore volume, mesoporous volume and pore diameter of the T-series samples are significantly greater than those of the C-series, further substantiating that the T-series possesses a more developed mesoporous framework, thereby reinforcing its hierarchical pore structure characteristics. It is noteworthy

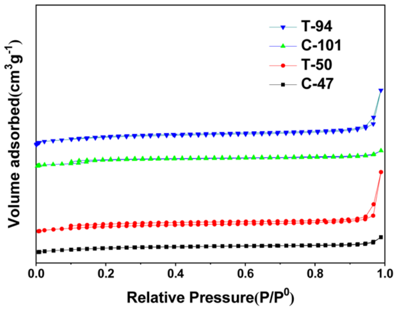

Fig. 5 N_2 adsorption–desorption isotherms of C-series and T-series ZSM-5 zeolites.

that the micropore volumes of all samples remained within the range of 0.146–0.152 cm^3 g^{-1}, showing minimal variation.

The ^{29}Si MAS NMR spectrum serves as an effective analytical tool for characterizing the states of silicon species within the zeolite framework. In the ^{29}Si MAS NMR spectrum, the main resonance peak of the chemical shift at −113 ppm and the resonance peak at −115 ppm are usually attributed to the Q^4 ($Si(OSi)_4$) structural unit, while the resonance peak at −103 ppm corresponds to Q^3 ($Si(OSi)_3OH$).[39,40] The Q^3 structure is indicative of defect sites in the zeolite framework, whereas the Q^4 structure represents silicon species in an isolated four-coordinated configuration. As shown in Fig. 6, both the C-series and T-series zeolites exhibit distinct signal peaks at −103.2 ppm and −113.2 ppm, confirming the coexistence of both Q^4 and Q^3 species in these materials. Specifically, the Q^4/Q^3 peak area ratios of ZSM-5 zeolites (C-101 and C-47) are 13.8 and 10.2, respectively, while those for ZSM-5 zeolites (T-94 and T-50) are 8.4 and 7.9, respectively. Compared to the T-series zeolites, the higher Q^4/Q^3 ratios observed in the C-series samples (C-101 and C-47) suggest that C-series zeolites possess fewer framework defects and demonstrate enhanced hydrophobic properties.

Literature investigations[32,33] demonstrate that in XPS analysis, the characteristic peak at a binding energy of 74.5 eV can be unambiguously assigned to the Al_{2p} orbital. As outlined in Section 2.2, the Si/Al molar ratios of the C-series (C-47, C-101) and T-series (T-50, T-94) samples are quantitatively determined to be 47, 101, 50, and 94, respectively, *via* ICP spectroscopy. Comparative analysis of the XPS data (Fig. 7) and Table S2 reveals corresponding measured Si/Al molar ratios of 53, 94, 105, and 254 for these samples. Notably, ICP analysis provides an assessment of the bulk chemical composition, whereas XPS characterizes the surface chemical state. The experimental findings indicate a substantial enrichment of silicon species on the surface of the T-series samples, as evidenced by their significantly higher surface Si/Al molar ratios relative to the bulk values. Conversely, the C-series samples exhibit negligible disparity between surface and bulk Si/Al molar ratios. This discrepancy underscores a pronounced silicon-rich surface characteristic in T-series ZSM-5 zeolites, while the C-series samples display an aluminium-enriched surface. Building upon these observations, further investigation into the aluminium atoms distribution in C-series ZSM-5 zeolites is conducted in conjunction with literature data. Prior research from our group[32,33] has conclusively demonstrated that highly cross-linked silicon species—particularly those exhibiting a "molecular gripper" effect—can effectively facilitate the homogeneous distribution of heteroatoms within the zeolite framework. Given that the C-series samples exhibit surface Si/Al molar ratios comparable to their bulk values, it can be logically deduced that the aluminium atoms of the C-series ZSM-5 zeolites synthesized using highly cross-linked silicon species also demonstrate a homogeneous distribution within the framework.

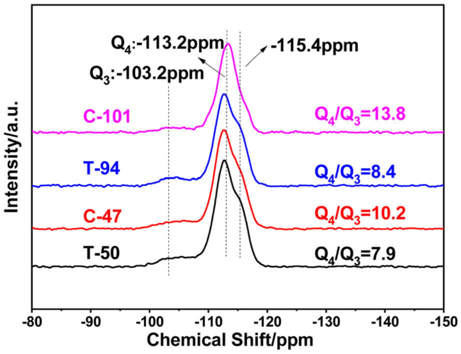

Fig. 6 ^{29}Si MAS NMR spectra of C-series and T-series ZSM-5 zeolites.

The spatial distribution of aluminium (Al) atoms within the framework pore system of ZSM-5 zeolites is systematically examined using ^{27}Al MAS NMR spectroscopy. As documented in the literature, the characteristic resonance peak at 56 ppm in the ^{27}Al MAS NMR spectrum is ascribed to framework Al species residing in the linear (straight) or sinusoidal channels of ZSM-5 zeolite, while the peak at 54 ppm is attributed to Al atoms situated at the intersection nodes of the pore channels.[41,42] As depicted in Fig. 8, both the T-series and C-series samples display distinct signal peaks at 54 ppm and 56 ppm, unequivocally confirming the coexistence of Al atoms in both the linear/sinusoidal pore regions and the pore intersection sites of these two zeolite variants. Specifically, the relative signal intensities at 54 ppm and 56 ppm are quantified as follows: 22% and 28% for the C-47 sample, 31% and 24% for the C-101 sample, 33% and 16% for the T-50 sample, and 32% and 22% for the T-94 sample. Comparative analysis reveals that the C-47 and C-101 samples exhibit a significantly higher proportion of signals at 56 ppm (28% and 24%, respectively) relative to the T-series samples (16% and 22%), indicative of a preferential enrichment of framework Al atoms within the linear or sinusoidal channels. Conversely, the T-50 and T-94 samples demonstrate a relatively elevated signal intensity at 54 ppm (33% and 32%, respectively) compared to their counterparts (22% and 31%), suggesting a greater accumulation of framework Al atoms at the pore intersection nodes.

Fig. 9 presents the NH_3-TPD characterization results of ZSM-5 zeolite. As reported in the literature,[43,44] the NH_3-TPD spectra of typical MFI-structured zeolites generally exhibit a bimodal distribution, wherein the low-temperature desorption peak (LT, ∼200–350 °C) and high-temperature desorption peak (HT,

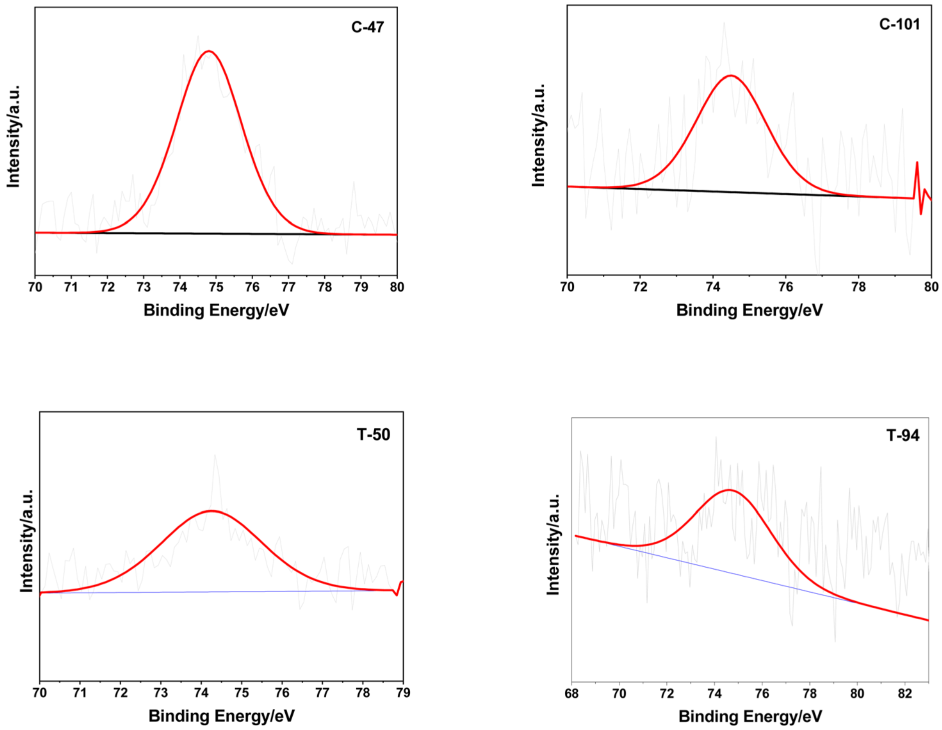

Fig. 7 XPS spectra of C-series and T-series ZSM-5 zeolites.

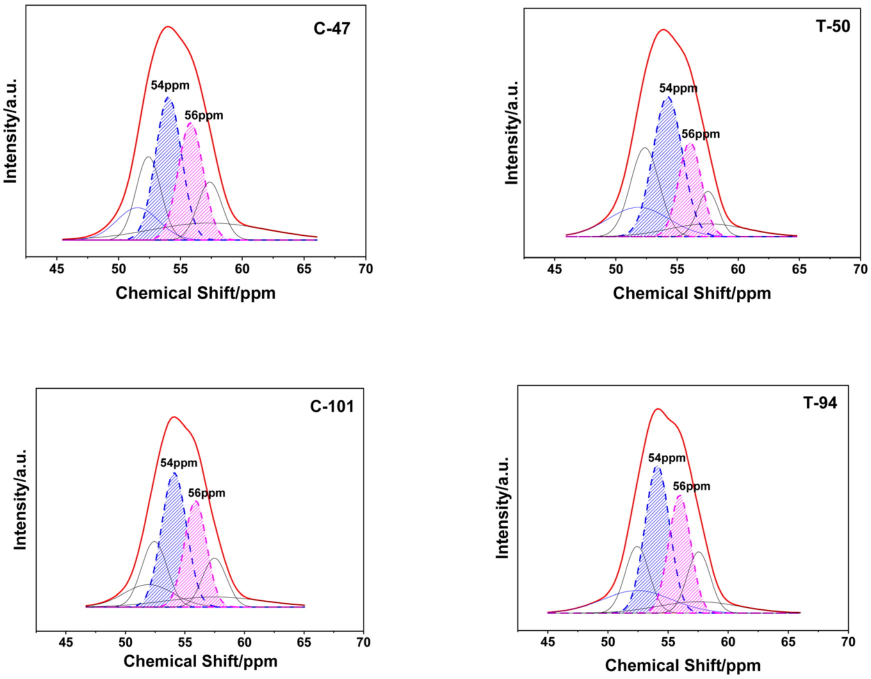

Fig. 8 ^{27}Al MAS NMR spectra of C-series and T-series ZSM-5 zeolites.

~350–500 °C) correspond to the adsorption of NH_3 molecules on weak and strong acid sites on the zeolite surface, respectively. As illustrated in Fig. 9, both the C-series and T-series ZSM-5 zeolites display distinct NH_3 desorption peaks in the low- and high-temperature regions. Notably, the NH_3-TPD curves of the T-series samples (T-94, T-50) exhibit prominent desorption peaks around 400 °C, whereas the desorption peak positions of the C-series samples (C-101, C-47) are markedly shifted toward the lower-temperature range (~380 °C). This observation suggests that the surface acid strength of the C-

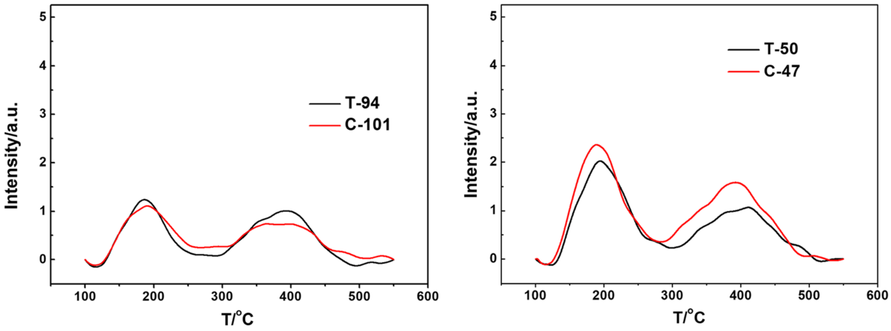

Fig. 9 NH_3-TPD profiles of C-series and T-series ZSM-5 zeolites.

series ZSM-5 zeolites is relatively weaker than that of the T-series zeolites.

Pyridine infrared (Py-IR) spectroscopy is employed to further investigate the acid properties of C-series and T-series ZSM-5 zeolites. Utilizing pyridine as a strong basic probe molecule, FT-IR adsorption spectroscopy enables effective characterization of both the acid density and strength of Brønsted and Lewis acid sites within the zeolites.[45–47] The spectral features are as follows: the pyridine-adsorbed band at 1545 cm^{-1} corresponds to Brønsted acid sites in ZSM-5 zeolites, while the band at 1454 cm^{-1} is attributed to Lewis acid sites. The desorption peak intensities at 150 °C correspond to the total contents of Brønsted and Lewis acid sites in the ZSM-5 samples, respectively. The strength of Brønsted acid centers in the ZSM-5 zeolites is semi-quantitatively evaluated by monitoring the pyridine desorption peak intensity at 1545 cm^{-1} (attributed to Brønsted acid sites) at different desorption temperatures (150 °C, 200 °C, 250 °C, 350 °C, and 450 °C), with normalization to the peak intensity at 150 °C. A more rapid decrease in the normalized intensity with increasing desorption temperature indicates weaker Brønsted acid strength in the ZSM-5 zeolite.[45–47] Based on the data from Fig. S2, Tables S3, and S4, normalization analysis is conducted to assess the population of Brønsted acid centers in the C-series and T-series ZSM-5 samples, as presented in Fig. 10. The results reveal that, compared to the T-series ZSM-5 zeolites, the normalized intensity of the C-series samples decreases more rapidly with increasing desorption temperature, suggesting a relatively weaker Brønsted acidity in the C-series zeolites. These Py-IR characterization findings in Fig. 10 are consistent with the NH_3-TPD results in Fig. 9, further confirming the lower acidity of the C-series zeolites.

3.3. ZSM-5 zeolites catalyzed 1-butene cracking reaction

The catalytic performance of ZSM-5 zeolite samples in the 1-butene cracking reaction is systematically investigated, with the experimental results comprehensively presented in Table 1. The findings demonstrate that, irrespective of whether considering the C-series or T-series products, an increase in the Si/Al ratio of the ZSM-5 zeolite leads to a notable reduction in both acid strength and acid density, consequently resulting in a decreased conversion rate of 1-butene. Notably, the C-series ZSM-5 zeolite exhibits a relatively lower 1-butene conversion rate compared to the T-series products, primarily attributable to its inherently weaker acid strength properties. This conclusion exhibits a high degree of consistency with the characterization results obtained from Py-IR and NH_3-TPD analyses.

Regarding the mechanism of the 1-butene cracking reaction,[18,48–50] the process primarily follows a typical bimolecular cracking pathway. Specifically, the reaction initiates with the double bond isomerization and skeletal isomerization of 1-butene, subsequently leading to the formation of a C_8-carbocation intermediate *via* butadiene dimerization. This key intermediate then undergoes further cracking reactions, predominantly yielding target products such as ethylene and propylene. Additionally, the primary cracking products participate in a series of complex secondary reactions, generating various by-products. Among these, C_3 alkanes are principally formed through hydrogen transfer reactions involving

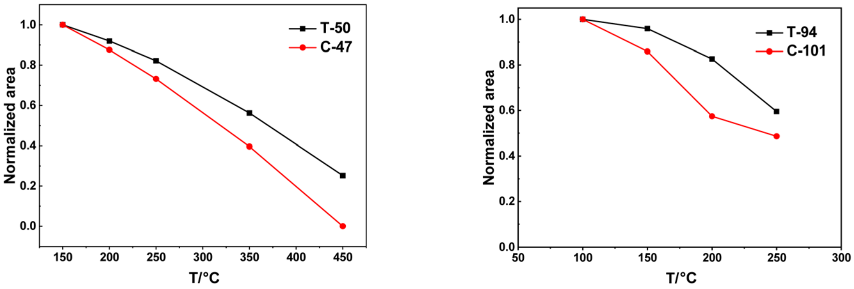

Fig. 10 Normalized area relative to Brønsted acid sites *versus* evacuation temperature over C-series and T-series ZSM-5 zeolites.

Table 1 Product distribution of butene cracking reaction catalyzed by ZSM-5 zeolite[a]

		Sel. (mol%)								
Zeolites	Conv. ($C_4^=$) (mol%)	$C_2^=$	$C_3^=$	$C_5^=$	$C_6^=$	$C_1^0 + C_2^0$	$C_3^0 + C_5^0$	H_2	Arom	P/E
C-101	69.88	12.28	55.09	12.92	5.64	0.31	11.75	0.61	1.21	4.49
T-94	77.01	17.32	50.14	7.73	4.22	0.82	14.96	1.24	3.33	2.89
C-47	82.10	19.39	38.79	5.84	4.01	1.52	22.34	2.10	5.70	2.00
T-50	88.93	19.18	26.25	3.01	4.30	3.25	28.97	4.96	9.78	1.37

[a] Reaction conditions: cat., 0.8 g; temperature, 500 °C; pressure, 0.1 MPa; 1-butene flow rate, 40 L min^{-1}; N_2 flow rate, 360 mL min^{-1}; WHSV, 7.50 h^{-1}; TOS, 1 h.

corresponding carbon-number cations; aromatic hydrocarbons and hydrogen are produced *via* the dehydrogenation–aromatization reaction pathway; methane and ethane originate from the side-chain cleavage reactions of isoparaffins and alkyl aromatic hydrocarbons; while C_5 olefins are generated through olefin oligomerization reactions or deprotonation processes of the corresponding carbocations.

Based on the product selectivity analysis (Table 1 and Fig. 11), it is observed that for both the T-series and C-series products, an increase in the Si/Al ratio of ZSM-5 zeolite results in a progressive decline in ethylene selectivity, concomitant with a corresponding rise in propylene selectivity. In the cracking process of C_4 olefins, ethylene is primarily derived from two pathways: (1) the direct cracking of C_8 carbocations, and (2) the subsequent cracking of shorter-chain carbocations (*e.g.*, C_5 and C_6 carbocations) generated from the initial C_8 carbocation cleavage. This indicates that the formation efficiency of ethylene is strongly influenced by the cracking activity of carbocations. As the Si/Al ratio of ZSM-5 zeolite increases, the reduced acidity leads to diminished carbocation cleavage activity, thereby decreasing ethylene selectivity with rising Si/Al ratio. In contrast, propylene generation depends not only on carbocation cracking but also on the deprotonation of C_3 carbocations, which likely plays a pivotal role in the enhanced propylene selectivity. Consequently, the combined effect of declining ethylene selectivity and increasing propylene selectivity leads to a marked elevation in the propylene-to-ethylene (P/E) ratio.

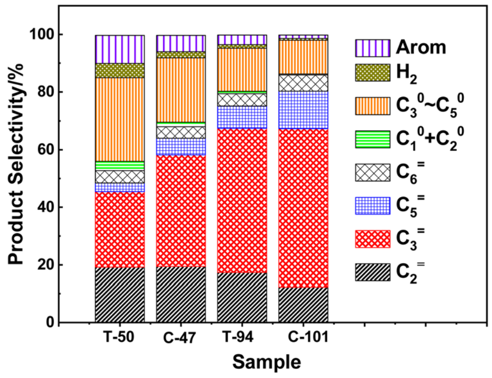

Fig. 11 Product distribution map of ZSM-5 zeolites catalyzed butene cracking reaction.

Further experimental observations indicate that with an increasing Si/Al ratio, the yields of alkanes, aromatics, and hydrogen exhibit a decreasing trend, whereas the selectivity toward C_5 alkenes demonstrates a notable enhancement. This phenomenon can be elucidated through the following mechanistic pathways: firstly, the overall acidity of the zeolite diminishes as the Si/Al ratio rises, accompanied by a reduction in the acid density of strong acid sites. Consequently, hydrogen transfer activity is significantly suppressed, leading to a decline in the selectivity of hydrogen transfer products (*e.g.*, C_3–C_5 alkanes). Secondly, methane and ethane primarily originate from side-chain cleavage reactions of branched alkanes or alkyl-substituted aromatic hydrocarbons. The decreased formation of aromatic products directly reduces the availability of these precursor species, thereby accounting for the observed reduction in methane and ethane selectivity. Thirdly, the diminished selectivity for aromatic hydrocarbons and hydrogen may stem from the reduced acid concentration resulting from the elevated Si/Al ratio. This decrease lowers the probability of interaction between intermediate species and acidic sites, consequently attenuating the activity of dehydrogenation–aromatization reactions. Lastly, the reduced acidity of the zeolite also weakens the cracking capability of carbocations, facilitating their direct conversion into olefinic products. This mechanistic pathway ultimately contributes to the enhanced yield of C_5 olefins.

In comparison to the catalytic performance of T-series ZSM-5 zeolites, C-series products demonstrate superior propylene selectivity and a higher propylene/ethylene (P/E) ratio in the 1-butene cracking reaction. Notably, the C-101 sample exhibits the optimal propylene selectivity and P/E ratio, underscoring the significant advantages of low Si/Al ratio ZSM-5 zeolites synthesized using highly cross-linked silicon species in catalyzing 1-butene cracking. These materials effectively enhance propylene selectivity while simultaneously suppressing aromatic and hydrogen formation. Characterization analysis indicates that this enhanced performance stems from the synergistic effects of several key factors: the C-series ZSM-5 zeolites possess moderate acidity, an Al-enriched surface, preferential distribution of framework Al atoms within the straight and sinusoidal channels, and an overall improved hydrophobic character.

As a widely recognized benchmark catalyst, ZSM-5 zeolite exhibits exceptional stability during the cracking of 1-butene ($C_4^=$), a performance attribute directly attributed to its unique three-dimensional microporous framework structure. Pioneering studies by Liu *et al.*[51] and Praserthdam *et al.*[52] have experimentally validated this stability, demonstrating that ZSM-5 maintains sustained catalytic activity for over 350 hours without noticeable deactivation during 1-butene cracking. Temperature-programmed oxidation (TPO) characterization further reveals that the primary cause of deactivation in ZSM-5 under these reaction conditions is the deposition of carbonaceous coke species, which gradually block the zeolite's pore channels and active sites over prolonged operation. This article proposes that ZSM-5 zeolite constructed with different cross-linked silicon species as structural elements should have significant structural specificity in terms of the evolution of catalytic life and deactivation mechanism. The structure–activity relationship of the C-ZSM-5 zeolite system in the C series is particularly noteworthy. Given the current research on the deactivation pathway analysis and lifetime regulation mechanism of ZSM-5 zeolite, there is an urgent need for in-depth exploration of related scientific issues.

4. Conclusions

This study systematically investigates the synthesis of ZSM-5 zeolites with distinct crosslinking degrees by modulating the alkalinity conditions during the dissolution of S-1 zeolite. Specifically, low and high alkalinity regimes are employed to prepare low-crosslinked and high-crosslinked silicon species, respectively, which serve as silicon sources for the subsequent synthesis of T-series and C-series ZSM-5 zeolites. Comprehensive characterization analyses reveal that, compared to the T-series counterpart, the C-series ZSM-5 zeolite demonstrates enhanced hydrophobicity and a higher surface aluminium content. The aluminium species in the C-series sample exhibit a preferential distribution within the straight and sinusoidal channels, accompanied by relatively weaker acid strength and reduced Brønsted (B) acid site density. These structural features collectively influence the catalytic performance in 1-butene cracking reactions: while the C-series zeolite shows a slightly lower 1-butene conversion rate, it delivers superior propylene selectivity, a higher propylene/ethylene (P/E) ratio, and minimized by-product formation. The findings provide valuable insights and theoretical guidance for optimizing industrial processes aimed at the highly selective conversion of 1-butene to propylene.

Author contributions

Z. Chen, X. Z. Dong and X. F. Chen carried out the syntheses, characterizations of the samples and writing – original draft. Z. Chen and J. F. Geng carried out the catalytic tests. Z. Chen, R. C. Rao and N. Li collected and analysed the FT-IR, ^{29}Si NMR and SEM data. Z. Chen and H. P. Zou collected and analysed the XRD, BET and ICP data. Z. Chen, R. C. Rao and W. H. Ou collected and analysed XPS, ^{29}Si MAS NMR and ^{27}Al MAS NMR data. Z. Chen was responsible for the overall direction of the project and preparation of the manuscript, with contributions from all authors.

Conflicts of interest

There are no conflicts to declare.

Data availability

All relevant data are within the manuscript and its supplementary information (SI). Supplementary information is available. See DOI: https://doi.org/10.1039/d5ra08160b.

Acknowledgements

We acknowledge support from the Introduction of High Level Talents Research Funding Project of Hefei Normal University (2023rcjj07), Jiangxi Qianyue New Materials Co., Ltd (22120101) and Anhui University collaborative innovation project (GXXT-2023-094). University level Research and Innovation Team Project of Hefei Normal University (2025KYTD16); Special Project for Promoting the Transformation of Scientific and Technological Achievements in Hefei Normal University (2025CGZH07).

References

1 H. C. Nerl, M. Plodinec and T. Gtsch, In situ formation of platinum-carbon catalysts in propane dehydrogenation, *Angew. Chem., Int. Ed.*, 2024, **63**, e202319887.
2 H. M. Torres Galvis and K. P. de Jong, Catalysts for production of lower olefins from synthesis gas: a review, *ACS Catal.*, 2013, **3**, 2130–2149.
3 M. H. M. Sofi, M. Y. S. Hamid and A. A. Jalil, Recent advancements of SAPO-34 and ZSM-5 zeolite in converting methanol to olefin: A review, *Arabian J. Sci. Eng.*, 2025, **50**, 3671–3697.
4 E. T. C. Vogt and B. M. Weckhuysen, Fluid catalytic cracking: recent developments on the grand old lady of zeolite catalysis, *Chem. Soc. Rev.*, 2015, **44**, 7342–7370.
5 N. Nishiyama, M. Kawaguchi and Y. Hirota, Size control of SAPO-34 crystals and their catalyst lifetime in the methanol-to-olefin reaction, *Appl. Catal., A*, 2009, **362**, 193–199.
6 W. Yan and N. Liu, Effect of Al-KIT-6 on self-metathesis of butene to propylene over supported tungsten-based catalyst, *Ind. Catal.*, 2022, **30**, 25–31.
7 T. Lu, Y. Sun and Z. Wang, Improved catalytic performance on post-treated zeolites SAPO-18 for 1-butene cracking, *Ind. Eng. Chem. Res.*, 2024, **63**, 11.
8 B. Wang, Q. Gao and J. Gao, Synthesis, characterization and catalytic C_4 alkene cracking properties of zeolite ZSM-23, *Appl. Catal., A*, 2004, **274**, 167–172.
9 G. Zhao, J. Teng and Y. Zhang, Synthesis of ZSM-48 zeolites and their catalytic performance in C_4-olefin cracking reactions, *Appl. Catal., A*, 2006, **299**, 167–174.
10 A. Miyaji, Y. Sakamoto and Y. Iwase, Selective production of ethylene and propylene via monomolecular cracking of pentene over proon-exchanged zeolites: Pentene cracking

mechanism determined by spatial volume of zeolite cavity, *J. Catal.*, 2013, **302**, 101–114.
11 B. Z. Qian, Superflex process for propylene production, *China Chem.*, 2001, **8**, 1.
12 T. V. Voskoboynikov, A. Y. Pelekh and J. J. Senetar, OCP catalyst with improved steam tolerance, *US Pat.*, 20110143919A1, 2011.
13 T. Taunoda and M. Sekiguch, The omega process for propylene production by olefin interconversion, *Catal. Surv. Asia*, 2008, **12**, 1–5.
14 J. W. Teng, G. L. Zhao and Z. K. Xie, Catalyst for olefin catalytic cracking to increase propylene production, *PCT*, 2004, **33**, 100–103.
15 G. L. Zhao, W. R. He and Z. Q. Yuan, Study on C_4 pyrolysis performance and carbon deposition of ZSM-5 zeolite, *PCT*, 2013, **42**, 6.
16 X. Zhu, S. Liu and Y. Song, Catalytic cracking of C_4 alkenes to propene and ethene: influences of zeolites pore structures and Si/Al_2 ratios, *Appl. Catal., A*, 2005, **288**, 134–142.
17 A. Kulkarni, A. Kumar and A. S. Goldman, Selectivity for dimers in pentene oligomerization over acid zeolites, *Catal. Commun.*, 2016, **75**, 98–102.
18 L. F. Lin, C. F. Qiu and Z. X. Zhuo, Acid strength controlled reaction pathways for the catalytic cracking of 1-butene to propene over ZSM-5, *J. Catal.*, 2014, **309**, 136–145.
19 X. Y. Zhang, F. Zhang and M. S. Zhang, Effect of acid distribution of ZSM-5 zeolite on the performance of butene pyrolysis to propylene, *PCT*, 2011, **40**, 926–931.
20 G. Zhao, J. Teng and Z. Xie, Effect of phosphorus on HZSM-5 catalyst for C_4-olefin cracking reactions to produce propylene, *J. Catal.*, 2007, **248**, 29–37.
21 Z. Wang, G. Jiang and Z. Zhao, Highly efficient P-modified HZSM-5 catalyst for the coupling transformation of methanol and 1-butene to propene, *Energy Fuels*, 2010, **24**, 758–763.
22 R. Xu, J. Liu and C. Liang, J. Effect of alkali metal ion modification on the catalytic performance of nano-HZSM-5 zeolite in butene cracking, *J. Fuel Chem. Technol.*, 2011, **39**, 449–454.
23 X. Zhu, S. Liu and Y. Song, Butene catalytic cracking to propene and ethene over potassium modified ZSM-5 Catalysts, *Catal. Lett.*, 2005, **103**, 201–210.
24 K. Wakui, K. Satoh and G. Sawada, Cracking of n-butane over alkaline earth-containing HZSM-5 catalysts, *Catal. Lett.*, 2002, **84**, 259–264.
25 N. Xue, N. Liu and L. Nie, 1-Butene cracking to propene over P/HZSM-5: Effect of lanthanum, *J. Mol. Catal. A: Chem.*, 2010, **327**, 12–19.
26 X. Wang, Z. Zhao and C. Xu, Effects of light rare earth on acidity and catalytic performance of HZSM-5 zeolite for catalytic cracking of butane to light olefins, *J. Rare Earths*, 2007, **25**, 321–328.
27 S. L. Burkett and M. E. Davis, Mechanism of structure direction in the synthesis of Si-ZSM-5: An investigation by intermolecular ^{1}H-^{29}Si CP MAS NMR, *J. Phys. Chem.*, 1994, **98**, 4647–4653.
28 J. Grand, H. Awala and S. Mintova, Mechanism of zeolites crystal growth: new findings and open questions, *CrystEngComm*, 2016, **18**, 650–664.
29 C. S. Cundy and P. A. Cox, The Hydrothermal synthesis of zeolites: History and development from the earliest days to the present time, *Chem. Rev.*, 2003, **34**, 663–702.
30 C. S. Cundy and P. A. Cox, The Hydrothermal synthesis of zeolites: precursors, intermediates and reaction mechanism, *Microporous Mesoporous Mater.*, 2005, **82**, 1–78.
31 L. Tosheva and V. P Valtchev, Nanozeolites: synthesis, crystallization mechanism, and applications, *Chem. Mater.*, 2005, **17**, 2494.
32 Z. Chen, X. Liu, Y. Yu, Z. Tang, J. Wang, D. Liu, N. Fang, Y. Lin, Y. Liu and M. He, Gripper-like silicon species for efficient synthesis of crystalline metallosilicates with spatially homogeneous heteroatoms in the framework, *Chem. Mater.*, 2021, **33**, 4988–5001.
33 Z. Chen, L. Zhang, Y. Yu, D. Liu, N. Fang, Y. Lin, D. Xu, F. Li, Y. Liu and M. He, TS-1 zeolite with homogeneous distribution of Ti atoms in the framework: synthesis, crystallization mechanism and its catalytic performance, *J. Catal.*, 2021, **404**, 990–998.
34 Z. Chen, L. Zhang, Y. Yu, D. Liu, N. Fang, Y. Liu and M. He, Molecular traffic control for catalytic oxidation reaction in TS-1 zeolite, *Microporous Mesoporous Mater.*, 2022, **332**, 111715.
35 Z. Chen, L. Wang, R. Rao, Y. Liu and H. Zou, An investigation on the effect of cross-linking state of silicon species on the distribution of framework Al atoms in ZSM-5 zeolite and its catalytic performance for MTO reaction, *Appl. Catal., A*, 2023, **65**, 119356.
36 M. M. J. Treacy and J. B. Higgins, *Collection of Simulated XRD Powder Patterns for Zeolites*, Elsevier, Amsterdam, 5th edn, 2007, p. 276.
37 H. Yu, X. Q. Wang and Y. C. Long, Synthesis of b-axis oriented high silica MFI type zeolite crystals introduced with co-template role, *Microporous Mesoporous Mater.*, 2006, **95**, 234–240.
38 Y. Tao, H. Kanoh and K. Kaneko, Comment: questions concerning the nitrogen adsorption data analysis for formation of supermicropores in ZSM-5 zeolites, *Adv. Mater.*, 2005, **17**, 2789–2791.
39 J. L. Guth, H. Kessler and R. Wey, New route to pentasil-type zeolites using a non alkaline medium in the presence of fluoride Ions, *Stud. Surf. Sci. Catal.*, 1986, **28**, 121–128.
40 O. Larlus and V. Valtchev, Control of the morphology of All-Silica BEA-type zeolite synthesized in basic media, *Chem. Mater.*, 2005, **17**, 881–886.
41 T. Biligetu, Y. Wang, T. Nishitoba, R. Otomo, S. Park, H. Mochizuki, J. Kondo, T. Tatsumi and T. Yokoi, Al distribution and catalytic performance of ZSM-5 zeolites synthesized with various alcohols, *J. Catal.*, 2017, **353**, 1–10.
42 T. Liang, J. Chen, Z. Qin, J. Li, P. Wang, S. Wang, G. Wang, M. Dong, W. Fan and J. Wang, Conversion of methanol to olefins over H-ZSM-5 zeolite: reaction pathway is related to the framework aluminum siting, *ACS Catal.*, 2016, **6**, 7311–7325.

43 J. G. Post and J. H. C. Van Hooff, Acidity and activity of H-ZSM-5 measured with NH_3-tpd and n-hexane cracking, *Zeolites*, 1984, **4**, 9–14.

44 W. E. Farneth and R. J. Gorte, Methods for characterizing zeolite acidity, *Chem. Rev.*, 1995, **95**, 615–636.

45 C. A. Emeis, Determination of integrated molar extinction coefficients for infrared absorption bands of pyridine adsorbed on solid acid catalysts, *J. Catal.*, 1993, **141**, 347–354.

46 B. Gil, S. I. Zones and S. J. Hwang, Acidic properties of SSZ-33 and SSZ-35 novel zeolites: a complex infrared and MAS NMR study, *J. Phys. Chem. C*, 2008, **112**, 2997–3007.

47 T. Barzetti, E. Selli and D. Moscotti, Pyridine and ammonia as probes for FTIR analysis of solid acid catalysts, *J. Chem. Soc., Faraday Trans.*, 1996, **92**, 1401–1407.

48 S. Zhao, D. Yang, X. Zhang, X. Yao, Y. Liu and M. He, ZSM-5 with controllable acidity as an efficient catalyst for a highly adjustable propene/ethene ratio in the 1-butene cracking, *Chem. Commun.*, 2016, **52**, 11191–11194.

49 T. Bi, Y. L. Chen, L. F. Lin and B. X. Han, Closed-loop recycling of polyethylene to ethylene and propylene via a kinetic decoupling–recoupling strategy, *Nat. Chem. Eng.*, 2025, **2**, 650–661.

50 R. Li, L. Y. Ma, Y. Li, C. M. Xu and J. W. Teng, Molecular kinetic model reveals isomerization-driven dimerization in *n*-butene catalytic cracking over HZSM-5, *Chem. Eng. Sci.*, 2026, **325**, 123406.

51 X. Huang, Y. X. Lin, B. H. Yan and Y. M. Liu, Deactivated TS-1 as an efficient catalyst for catalytic cracking of butene to propene, *CIESC J.*, 2021, **72**, 5183–5195.

52 C. Auepattana-aumrung, K. Suriye, B. Jongsomjit, J. Panpranot and P. Praserthdam, Inhibition effect of Na^+ form in ZSM-5 zeolite on hydrogen transfer reaction via 1-butene cracking, *Catal. Today*, 2020, **358**, 237–245.